Research Square

Preprints are preliminary reports that have not undergone peer review.
They should not be considered conclusive, used to inform clinical practice,
or referenced by the media as validated information.

Controlling Molecular Nanomagnet Properties by the Host Lattice

Joscha Nehrkorn
Max Planck Institute for Chemical Energy Conversion
Igor Valuev
International Tomography Center SB RAS https://orcid.org/0000-0002-1799-000X
Artem Bogomyakov
International Tomography Center SB RAS
Elizaveta Suturina
University of Bath
Alena Sheveleva
University of Manchester https://orcid.org/0000-0001-6190-5944
Victor Ovcharenko
International Tomography Center SB RAS
Karsten Holldack
Helmholtz-Zentrum Berlin https://orcid.org/0000-0003-3931-3971
Carmen Herrmann
University of Hamburg https://orcid.org/0000-0002-9496-0664
Matvey Fedin
International Tomography Center SB RAS
Alexander Schnegg (alexander.schnegg@cec.mpg.de)
Max Planck Institute for Chemical Energy Conversion https://orcid.org/0000-0002-2362-0638
Sergey Veber
International Tomography Center https://orcid.org/0000-0002-5445-3713

Article

Keywords: molecular nanomagnets, molecule-based magnetic materials, host lattice

Posted Date: August 24th, 2020

DOI: https://doi.org/10.21203/rs.3.rs-57027/v1

License: This work is licensed under a Creative Commons Attribution 4.0 International License.
Read Full License

Controlling Molecular Nanomagnet Properties by the Host Lattice

Joscha Nehrkorn,[1,2,3,4,†] Igor A. Valuev,[5,6,†] Mikhail A. Kiskin,[7] Artem S. Bogomyakov,[5,6] Elizaveta A. Suturina,[6,8] Alena M. Sheveleva,[5,6] Victor I. Ovcharenko,[5] Karsten Holldack,[1] Carmen Herrmann[3], Matvey V. Fedin,[5,6] Alexander Schnegg,[1,4,*] and Sergey L. Veber[5,6,*]

[1]Helmholtz-Zentrum Berlin für Materialien und Energie, Berlin, Germany

[2]Department of Chemistry, University of Washington, Seattle, WA, United States

[3]Institut für Anorganische und Angewandte Chemie, Universität Hamburg, Hamburg, Germany

[4]Max Planck Institute for Chemical Energy Conversion, Mülheim/Ruhr, Germany

[5]International Tomography Center SB RAS, Novosibirsk, Russia

[6]Novosibirsk State University, Novosibirsk, Russia

[7]N.S. Kurnakov Institute of General and Inorganic Chemistry, Moscow, Russia

[8]Department of Chemistry, University of Bath, Claverton Down, Bath, BA2 7AY, UK

[*]e-mail: sergey.veber@tomo.nsc.ru, alexander.schnegg@cec.mpg.de

[†]These authors contributed equally.

ABSTRACT

Structural control over the magnetic properties of molecular nanomagnets (MNM) is key to bottom up design strategies for novel molecule-based magnetic materials, for e.g. data storage, magnetic cooling or spintronics. Herein, we switch the magnetism of materials made of the single-molecule magnet $[Co_xZn_{(1-x)}(piv)_2(2\text{-}NH_2\text{-}Py)_2]$, by structural changes induced by gradual replacement of complexes containing paramagnetic Co(II) with analogues containing diamagnetic Zn(II). Combining advanced structural and magnetic characterization techniques, we show that a change of the ratio of the two ions induces a change of the Co(II) coordination structure, changed magnetic relaxation times and a switch from easy-plane to easy-axis type magnetic anisotropy. Complementary quantum chemical calculations reveal magneto structural correlations, rationalizing the structural origin of the changed magnetic properties upon magnetic dilution. This approach provides an important new lever to understand, predict and tune the magnetic properties of a large range of MNM based magnetic materials.

Magnetic materials play a crucial role in information storage, communication, medical technologies and many other areas essential to modern societies. Driven by the demand for ever smaller magnetic units and the quest for magnetic materials with new properties, novel magnetic materials derived from molecular nanomagnets (MNMs) are intensively explored.[1–3]

MNMs exhibit fascinating magnetic properties, which are relevant for a plethora of potential applications like magneto-caloric cooling,[4] single molecule based data storage[5,6] (*e.g.* with single-molecule magnets), entanglement,[7] quantum computing[8,9] (*e.g.* molecular qubits or qudits) and other molecular spintronics applications.[10–12]

MNM properties are decisively determined by the anisotropy of the magnetic moment, defined by a unique axis. Orienting the magnetic moment along this axis is energetically favorable or adverse, which is referred to as easy-axis or easy-plane anisotropy, respectively. Strong anisotropy is considered a necessary criterion for a single-molecule magnet. In contrast, weak anisotropy is favorable for magneto-caloric cooling. Control over the magnetic anisotropy is therefore key to the rational design of MNM based magnetic materials.

Anisotropy is subtly determined by the coordination environment and the electronic structure of the complex.[13] Hence, alternation of the coordination structure affects the magnetic properties. In most cases, these changes are realized by ligand exchange, which usually does not allow for predictable fine-tuning of the magnetic properties.[14–21] This urges for more gradual methods to adjust magnetic anisotropies.

Transition metal ion complexes are an ideal platform for knowledge-based MNM design strategies, due to the accumulated insight in their magneto-structural correlations.[1,22] Significant attention in this context has been devoted to Co(II), where large first order spin-orbit coupling (SOC) can lead to very large anisotropies.[1,23–25] An increasing number of Co(II) complexes have been reported, which exhibit slow relaxation of the magnetization.[26,27] In most of these single molecule magnets slow relaxation of the magnetization is observed in the

presence of an external magnetic field, with a few prominent exceptions exhibiting slow relaxation already at zero magnetic field.[26,27]

In addition to their appealing individual magnetic properties, MNMs allow for bottom-up design of novel 1D, 2D and 3D magnetic materials from molecules. For the design of future MNM-based devices, both aspects, control of the anisotropy as well as their integration in application-friendly matrices, are of paramount importance. However, established synthesis approaches, for apparent reasons, address these aspects independently.

Herein, we report the successful application of an integrated approach, where the anisotropy of a Co(II) MNM is switched from easy-plane to easy-axis by intentionally varying the host lattice. It is demonstrated by X-ray diffraction that exchange of paramagnetic Co(II) (S = 3/2) against diamagnetic Zn(II) in crystals composed of $[Co_xZn_{(1-x)}(piv)_2(2\text{-}NH_2\text{-}Py)_2]$ ($\mathbf{1}_x$, with x = 1, 0.9, 0.75, 0.5, 0.25, 0.1, 0.03, 0.01, 0) alters the coordination geometry from distorted octahedral to distorted tetrahedral. This structural change is accompanied by an increase of the magnetization relaxation time by more than five times. Structure induced changes of the equilibrium magnetic properties are determined by electron paramagnetic resonance (EPR) experiments at X-band (9.4 GHz) and THz frequencies. Thereby, we are able to unequivocally identify a switch from easy-plane to easy-axis anisotropy. The observed changes in the magnetic properties are correlated to the geometric structure by quantum chemical calculations.

Single-crystal structures were obtained for samples $\mathbf{1}_x$ with x = 1, 0.9, 0.75, 0.5, 0.25, 0.1 and 0. Pure Co(II) and Zn(II) crystals ($\mathbf{1}_1$ and $\mathbf{1}_0$, respectively) crystallize in the monoclinic space group $P2_1/c$, but with different cell parameters (see Table S2). Structures of the pure compounds $\mathbf{1}_1$ and $\mathbf{1}_0$ are depicted in Figures 1b and 1a, respectively. In $\mathbf{1}_1$, the metal ion was observed in a distorted octahedral ligand environment. The corresponding shape measure[28] is $S_Q(O_h)$ = 4.12. The ligand environment for $\mathbf{1}_0$ is closer to tetrahedral, with $S_Q(T_d)$ = 1.03. Fig. 1 shows changes in structure and magnetic properties induced by gradual dilution. It displays the bond length

from the metal to one of the coordinating oxygen atoms and the spin ground state splitting Δ *vs.* Co(II) concentration.

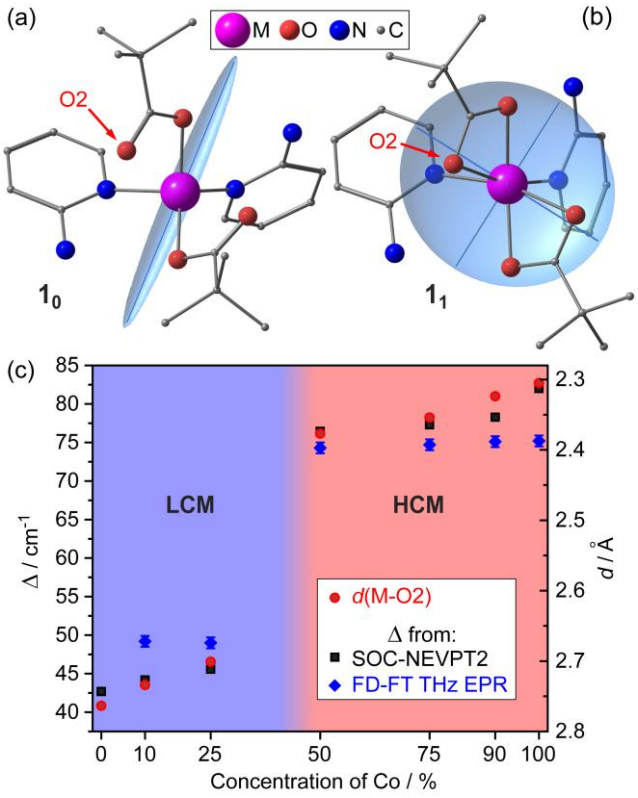

Figure 1: Host matrix induced changes of the ligand structure affect Co(II) magnetic anisotropy in Co depleted (LCM) and Co rich (HCM) materials. Molecular structures of $\mathbf{1_0}$ (a) and $\mathbf{1_1}$ (b), where M refers to the metal (either Co or Zn). Tensors representing the anisotropic response of the ground state Kramers doublet to a magnetic field as calculated by SOC-NEVPT2 are shown in light blue. In $\mathbf{1_1}$ the metal ion has a distorted octahedral coordination environment and easy-plane anisotropy (*i.e.* an oblate tensor). $\mathbf{1_0}$ features a tetrahedral coordination environment and easy-axis anisotropy (prolate tensor). (c) Zero-field splitting Δ extracted from FD-FT THz-EPR experiments and calculated by SOC-NEVPT2. A steep increase of Δ with increasing Co(II) concentration can be observed around 50 % concentration. This anisotropy change correlates with bond lengths between the metal ion and the atoms in the first ligation shell. The bond length between metal and oxygen atom O2 is shown (red circles and *y*-scale on the right). Related plots for the remaining atoms in the first coordination shell are shown in the SI (see Table S3 and Figures S1 & S33).

All samples except $\mathbf{1_{0.5}}$ crystallize in one crystalline phase according to Powder X-ray diffraction (PXRD) (see Figures S2–S9). For $\mathbf{1_{0.5}}$, two phases contributing with 92 % and 8 % were observed (see Figure S5). In this case, only the predominant phase is further considered. A gradual decrease of Co(II) concentration in $\mathbf{1_1}$, $\mathbf{1_{0.9}}$, $\mathbf{1_{0.75}}$, and $\mathbf{1_{0.5}}$ leads to modest changes in bond lengths. By contrast, severe changes are observed for a further decrease of Co(II) concentration from $\mathbf{1_{0.5}}$ to $\mathbf{1_{0.25}}$. The resulting structure is very similar to $\mathbf{1_{0.1}}$ and $\mathbf{1_0}$. Hence, in the further discussion we distinguish between the two groups as high-concentration materials

(HCM), **1**$_1$, **1**$_{0.9}$, **1**$_{0.75}$, and **1**$_{0.5}$, and low-concentration materials (LCM), **1**$_{0.25}$, **1**$_{0.1}$, **1**$_{0.03}$, **1**$_{0.01}$ (the latter two were only studied by X-band EPR). Further structural details can be found in the SI.

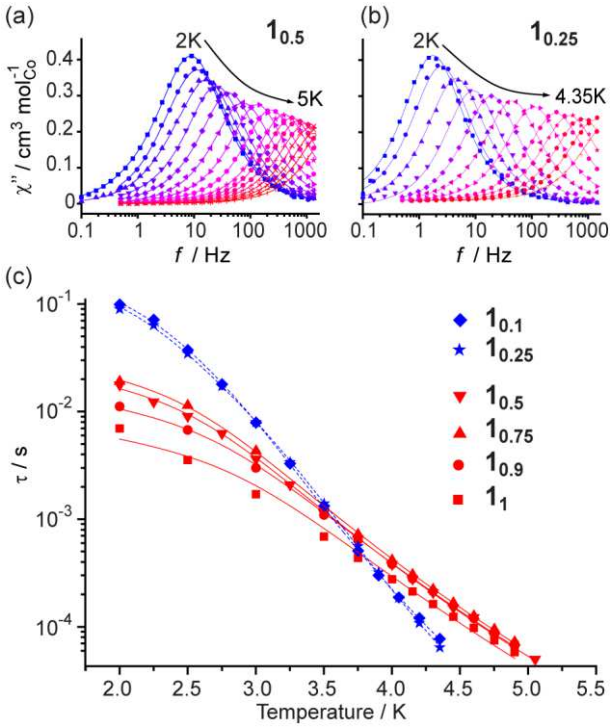

Figure 2: AC susceptibility data reveal a clear correlation between magnetic relaxation properties and magnetic anisotropies in HCM and LCM. (a) and (b) depict out-of-phase AC susceptibility traces, χ'', *vs.* frequency, *f*, for **1**$_{0.5}$ and **1**$_{0.25}$. (c) Extracted relaxation times τ show different temperature dependencies for LCM (blue symbols) and HCM (red symbols).

Many MNM applications are determined by the relaxation times of their magnetization. This property can be conveniently quantified by AC susceptibility measurements.[29] For **1**$_1$, **1**$_{0.9}$, **1**$_{0.75}$, **1**$_{0.5}$, **1**$_{0.25}$ and **1**$_{0.1}$ out-of-phase AC susceptibilities were measured under an applied DC field of 200 mT. Subsequently relaxation times τ were determined (see Figure 2 and SI). A striking difference in the temperature dependence of τ was observed for LCM *vs.* HCM. Least square fits to the inverse relaxation times (see SI for details) indicate that Raman and direct processes dominate for HCM.[30] This model was not sufficient to describe the relaxation in LCM, where an additional Orbach process[31] had to be included to reach satisfying agreement between simulation and experiment. The increase in relaxation with increasing Co(II) concentration within the LCM and HCM groups can be tentatively assigned to an increase of the intermolecular spin-spin interactions.

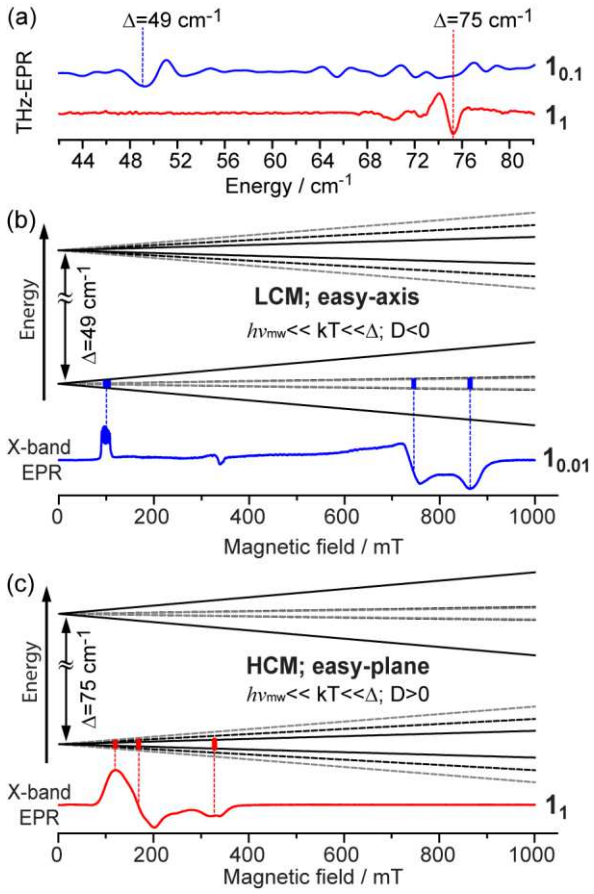

Figure 3: EPR allows for assigning magnitude and sign of the magnetic anisotropy of LCM and HCM. (a) THz-EPR quantifies Δ = 75 cm^{-1} and Δ = 49 cm^{-1} for HCM (red) and LCM (blue), respectively. Δ is the energy gap between ground-state and excited-state doublets without external magnetic field, see (b) and (c). (b) Depicts magnetic field dependent S = 3/2 energy levels for easy-axis (D < 0) anisotropy alongside LCM X-band EPR spectra (blue trace). Ground-state and excited-state doublets are plotted for magnetic fields parallel to the main anisotropy axis (solid black lines) and perpendicular to it (black and gray dashed lines). Resonance magnetic fields are assigned to the corresponding EPR transitions by blue dashed lines. (c) Orientation dependent spin energy levels and HCM X-band EPR spectrum (red trace) for easy-plane (D > 0). Resonance fields are assigned to EPR transitions by red dashed lines.

Equilibrium magnetic properties are essential to understand dynamic magnetic properties, like relaxation of the magnetization. Further, they are linked to the geometric and electronic structure via spin-orbit interaction. For the case of Co(II) (S = 3/2), the equilibrium magnetic properties are determined by the ground state Kramers doublet and the energy difference Δ to the first excited Kramers doublet (see Figure 3 and SI). EPR is the method of choice to probe the transition energies between these levels. However, the relevant energies span several orders of magnitude. We therefore combined very broadband THz-EPR and X-band EPR. THz-EPR allows for direct detection of Δ, which is hardly possible with other methods.[25,32–34] On the contrary, X-band EPR ($h\nu_{\mathrm{X-band}} \approx 0.33$ cm$^{-1} \ll \Delta$) detects transitions within the ground state doublet, which are most sensitive to the rhombicity and the type of anisotropy.[35]

THz-EPR revealed Δ = 75 cm^{-1} and Δ = 49 cm^{-1} for HCM and LCM, respectively (see Figure 3a) and the SI for further data). X-band EPR on HCM exhibit essentially all identical resonance fields of 115 mT, 170 mT, and 325 mT, while for LCM resonance fields at 100 mT, 745 mT, and 875 mT were observed (see Figure 3b and 3c, dashed vertical lines). Although the spectral shapes vary widely for LCM, the observed resonance fields were similar (see Figure S24). The observed resonance fields directly indicate easy-plane anisotropy for HCM and easy-axis anisotropy for LCM. In both series, the line width increases with increasing Co(II) concentration, which is tentatively assigned to an increase of dipolar spin-spin interactions.

We use, for the sake of simplicity, an effective spin S = 3/2 Hamiltonian for the simulation of EPR spectra.

$$\widehat{H}_{3/2} = D\left(\hat{S}_z^2 - \tfrac{1}{3}\widehat{\boldsymbol{S}}^2\right) + E\left(\hat{S}_x^2 - \hat{S}_y^2\right) + \mu_B \boldsymbol{B}_0 \cdot \boldsymbol{g} \cdot \widehat{\boldsymbol{S}} \qquad (1)$$

The first and the second terms account for the zero-field splitting (ZFS), with the axial and rhombic ZFS parameters D and E, respectively. By definition, $0 \leq E/D \leq \frac{1}{3}$, and the z-axis is the unique anisotropy axis. For positive D, this is the hard axis, and for negative D the easy axis. The energy difference between the doublets is $\Delta = 2\sqrt{D^2 + 3E^2}$. The third term in equation 1 is the anisotropic Zeeman interaction, where the $\boldsymbol{g}$-tensor is assumed to be diagonal and axial, *i.e.* $\boldsymbol{g} = \mathrm{diag}(g_\perp, g_\perp, g_{||})$.

The following parameters were found to reliably model the EPR data:

HCM: D = 36.7 cm^{-1}, E = 4.5 cm^{-1}, $g_\perp$ = 2.53, $g_{||}$ = 2.21

LCM: D = -23.9 cm^{-1}, E = 3.1 cm^{-1}, $g_\perp$ = 2.25, $g_{||}$ = 2.38

The final missing link between the geometric and electronic structures on the one hand and the magnetic properties on the other hand is accessible through quantum chemical calculations.[24,36] *Ab initio* calculations were performed for a single molecule with Co(II) in the experimentally

obtained structures of $\mathbf{1_1}$, $\mathbf{1_{0.9}}$, $\mathbf{1_{0.75}}$, $\mathbf{1_{0.5}}$. $\mathbf{1_{0.25}}$, $\mathbf{1_{0.1}}$ and (the fictitious) $\mathbf{1_0}$. Calculated Δ were 82 cm^{-1}, 78 cm^{-1}, 77 cm^{-1}, 76 cm^{-1}, 45 cm^{-1}, 44 cm^{-1} and 43 cm^{-1}, respectively. These values match the experimental results very well. The trends in the calculated Δ can be directly assigned to trends in the bond lengths (see Fig. 1c and SI). This is a tempting correlation. However, the bond lengths are an average over the crystal and do not necessarily reflect the bond lengths in the individual Co(II) molecule (see SI for a more detailed discussion). In the following, $\mathbf{1_1}$ is discussed as representative for HCM and $\mathbf{1_0}$ for LCM. Calculated tensors of magnetic anisotropy of the ground doublet state (see Fig. 1a, b and SI) show clear difference: it is oblate for $\mathbf{1_1}$ and prolate for $\mathbf{1_0}$, hence they have easy-plane and easy-axis anisotropy, respectively. In a simplified model, contributions of orbital states to the calculated D values (Table S11) were analyzed.[22,24] For $\mathbf{1_1}$, the first and second excited states contribute significantly. They can be mixed with the ground state by the operators $\hat{L}_x$ and $\hat{L}_y$, but not by $\hat{L}_z$, therefore D is positive. In $\mathbf{1_0}$, the first excited state has the main contribution to D, and this state can be mixed with the ground state only by $\hat{L}_z$, resulting in negative D.

Based on the assignment of the anisotropy, the dynamics of the magnetization may be rationalized. We observed vastly different magnetic properties for HCM and LCM, while inside each group the magnetic properties were found, basically, identical. HCM showed significant easy-plane anisotropy. For this type of anisotropy, the energy barrier for reorientation of the magnetization from one ground state to the other vanishes. Indeed, we could fit the (inverse) relaxation times obtained by AC susceptibility without account of any barriers and related processes, and this additionally supports the easy-plane anisotropy. Similar arguments hold for LCM with easy-axis anisotropy. An Orbach process, *i.e.* thermal relaxation over an energy barrier, had to be included to describe AC susceptibility results.

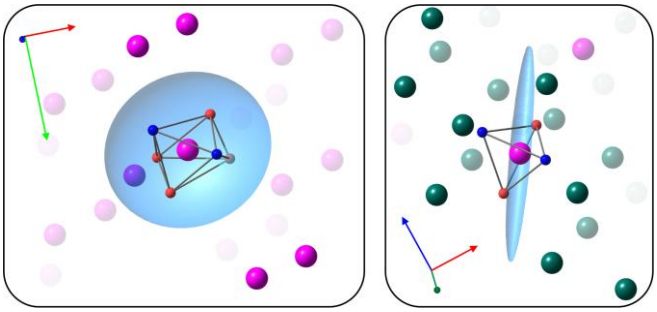

Figure 4: Schematic view of Co(II) (blue spheres) surrounded by other Co(II) (left, HCM) and Zn(II) (black spheres, right, LCM). In HCM, all or the majority of complexes contain Co(II), with distorted octahedral ligand environment and easy-plane type of anisotropy, depicted by an oblate tensor. In the LCM counterparts complexes molecules containing Co(II) are a minority. The remaining Co(II) are in a distorted tetrahedral ligand environment, resulting in easy-axis magnetic anisotropy (prolate tensor). Differences in the crystal packing and the size of the unit cell are indicated by different box sizes.

In summary, we report a new way to influence MNM properties by the host lattice. By forming a diamagnetically diluted crystal lattice with slight structural mismatch, we were able to drastically change the magnetic properties of MNM based magnetic materials (see Figure 4). The *ab initio* calculations, which reproduce the change of the magnetic properties upon replacement of Co(II) with Zn(II), underline the great potential of this approach. These calculations hint towards direct correlation between the concentration dependent ligand bond lengths and the zero-field splittings Δ. The degree of control and understanding gained through sample preparation, spectroscopy and quantum chemical calculations demonstrates that a comprehensive approach is required for the design of new magnetic materials. These findings can pave new ways to optimize MNM properties, without changing the ligands. Such an approach may be ideally combined with state-of-the-art machine learning approaches aiming for computer aided optimization of MNM materials.[37] Furthermore, structural modifications induced by altering the MNM host lattice are comparably subtle, since the ligand environment changes only geometrically.

Our work enables new approaches to switch and control the magnetic anisotropy by external stimuli (e.g. light, pressure or potential bias).[38–41] We show that by matrix embedding, an MNM can be tuned to a regime where slight structural changes lead to drastic changes of the anisotropy from easy-plane to easy-axis type. It is tempting to propose magnetic materials in

208 which the magnetic properties can be switched by temperature or pressure beyond the range
209 that has been demonstrated.[42,43] This opens up new routes for the design of molecular devices,
210 like magnetic memory units, cooling units, switches, sensors, or actuators. While our work is
211 focused on Co(II) and Zn(II) molecules it is clear that it can be applied to any para-/diamagnetic
212 pair of chemically similar elements. Hence, our approach can be straightforwardly applied to
213 other transition metals and lanthanides.

214 ## Methods

215 Crystalline materials of the complexes $[Co_xZn_{(1-x)}(piv)_2(2\text{-}NH_2\text{-}Py)_2]$ (**1**$_x$, with x = 1, 0.9, 0.75,
216 0.5, 0.25, 0.1, 0.03, 0.01, 0) were obtained according to procedures described elsewhere for
217 **1**$_1$;[44] and in the SI. Powder X-Ray Diffraction (PXRD) was performed on a Bruker D8
218 instrument (Cu-Kα radiation). Infrared (IR) spectra in the range 400–4000 cm^{-1} were measured
219 on a Fourier-Transform IR (FT-IR) Perkin Elmer Spectrum-65LS spectrometer with Specac's
220 high performance single reflection monolithic diamond attenuated total reflection (ATR)
221 accessory. Elemental analysis was carried out on an EA1108 Carlo Erba automatic CHNS-
222 analyzer. Energy-dispersive X-ray (EDX) analysis was performed in the mapping mode on an
223 Oxford Instruments X-MAX EDX analyzer for the determination of Co:Zn ratios.

224 Diffraction data for all complexes was collected on a Bruker SMART APEX II diffractometer
225 equipped with a charge-coupled device (CCD) detector (graphite monochromator,
226 λ(MoKα) = 0.71073 Å).[45] Absorption correction was applied based on the intensities of
227 equivalent reflections with the SADABS program.[46] The structures of all compounds were
228 solved by the direct method and refined by the full-matrix least squares technique in the
229 anisotropic approximation (except hydrogen atoms) using the SHELX-2014 software. The
230 positions of the hydrogen atoms in the organic ligands were calculated geometrically and
231 refined in the riding model (in some structures H atoms in NH_2-groups could be located by
232 Fourier maps).

AC magnetic susceptibility data was collected on a Quantum Design MPMS-XL SQUID magnetometer on finely ground polycrystalline powders (~20 mg) in the temperature range of 2-5 K under a DC field of 0.2 T and an AC field of 0.35 mT oscillating in a frequency range of 0.1-1500 Hz.

Frequency Domain Fourier Transform THz EPR (THz-EPR) at external magnetic fields from 0 to 10 T was performed at the THz beamline of the synchrotron radiation facility BESSY II in Voigt configuration and with a Hg arc lamp as THz source.[32,47,48] THz-EPR samples were prepared as pellets containing typically 20 mg of $\mathbf{1}_x$ mixed with approximately 100 mg of polyethylene powder. Experiments were performed at low temperatures. If not stated otherwise, the temperature was 5 K. Experimental resolution was 0.2 cm^{-1} (experiments on $\mathbf{1}_1$ and $\mathbf{1}_{0.1}$) or 1 cm^{-1} (all other samples). A 6 μm Mylar Multilayer beam splitter was used and the signals were detected with a 4.2 K Si bolometer (Infrared Laboratories). THz-EPR spectra are shown as magnetic field division spectra (MDS), obtained by dividing spectra measured at an external magnetic field B_0 by a reference spectrum measured at B_0+ 1 T.[32]

Continuous wave (CW) X-band (9.7 GHz) EPR measurements were carried out on a Bruker Elexsys E580 spectrometer, equipped with an Oxford Instruments He cryostat (ER 4118CF-O) and temperature controller ITC 503S. A Bruker ER 4118X-MD5 resonator was modified by replacing the dielectric sapphire insert by bismuth germanate (3 mm inner diameter) to suppress the resonator background.[49] X-band EPR spectra were recorded at a microwave power of ~1.9 mW and a Lock-In modulation amplitude of 0.5 mT. X-band EPR samples of $\mathbf{1}_x$ with Co(II) amounts $x = 1 \div 0.1$ were ground and mixed with quartz powder. For each sample the quantity of quartz was approximately 20 mg, the amount of $\mathbf{1}_x$ increased from ~2 mg to ~10 mg upon decreasing x. Samples with $x = 0.03$ and 0.01 were ground and used without additions. The weighted quantity of ground samples (~15 mg, polycrystalline powder) was placed in a 2.8 mm

outer diameter EPR tube, evacuated (10^{-2} mbar) and fused. Both, THz-EPR and X-band EPR data was simulated with the *EasySpin* toolbox.[50–52]

State-averaged complete active space self-consisted field (SA-CASSCF) [53–55] calculations were performed using experimentally obtained structures (always assuming a Co atom at the metal position, irrespective of the value of x) without further geometry optimizations. The segmented all-electron relativistically contracted version[56] of Ahlrichs polarized basis set def2-TZVP was used.[57–59] To speed up calculations, the resolution of identity approximation with corresponding correlation fitting of the basis set was employed.[60] Dynamic correlations and scalar relativistic effects were taken into account by N-electron valence perturbation theory to second order (NEVPT2),[61,62] and by the second-order Douglas-Kroll-Hess (DKH) procedure,[63,64] respectively. The complete active space CAS (7, 5) contained seven electrons in five d-orbitals. All 10 quartet and 40 doublet states of Co(II) were included. The fine structure of ground and excited states were computed within the Breit-Pauli approximation and the mean field approximation (SOMF).[65] Spin Hamiltonian (SH) parameters and g-factors have been computed by second order perturbation theory (PT2)[66] and with an effective Hamiltonian (QDPT).[65,67] All quantum chemical calculations were performed with the ORCA computational program package.[68]

Acknowledgements

Financial support by the Russian Science Foundation through grant no. 17-13-01412 (X-band EPR measurements) and by the Deutsche Forschungsgemeinschaft (DFG) through priority program SPP 1601 and a Research Fellowship to J.N. (grant no. NE 2064/1-1 FOR) is thankfully acknowledged. J.N., I.A.V., and S.L.V. thankfully acknowledge the financial support from HZB. J.N. and A.S. acknowledge funding through the Max Planck Society. M.A.K. is grateful for financial support from the State Assignment on Fundamental Research of the Kurnakov Institute of General and Inorganic Chemistry of RAS (IGIC RAS) and thank

the User Facilities Centers of IGIC RAS for the facility to do X-ray, IR and elemental analysis measurements. V.I.O. and A.S.B. acknowledge Russian Science Foundation (project 18-13-00380) for support of the SQUID measurements. E.A.S acknowledges Russian Science Foundation (project 16-13-10155) and Supercomputer center of the Novosibirsk State University for support of the computational part of this work. J.N. and C.H. thank the University of Hamburg High Performance Computing Centre (RRZ) for computational resources. We thank Dirk Ponwitz (HZB) for technical support, Dr. Ekaterina Zorina-Tikhonova (IGIC RAS) for IR data interpretation and Dr. Alexander Baranchikov (IGIC RAS) for EDX analysis.

Author contributions

S.L.V. and J.N. conceived the research. M.A.K. synthesized the molecules, performed chemical characterizations and X-ray analyses. I.A.V., A.S.B., V.I.O., S.L.V. performed and analyzed AC susceptibility experiments. I.A.V., A.M.S., M.V.F. and S.L.V. performed and analyzed the X-Band EPR experiments. J.N., I.A.V., K.H., and S.L.V. performed the THz-EPR experiments with support of A.S. J.N., with support of C. H., and E.A.S. performed and analyzed ab initio calculations. J.N., A.S, M.V.F, E.A.S, and S.L.V. wrote the manuscript with contributions from all authors. A.S. and S.V. oversaw the project.

References

1. Frost, J. M., Harriman, K. L. M. & Murugesu, M. The rise of 3-d single-ion magnets in molecular magnetism: Towards materials from molecules? *Chemical Science* **7**, 2470–2491 (2016).

2. Cornia, A. *et al.* Preparation of novel materials using SMMs. in *Structure and Bonding* **122**, 133–161 (Springer-Verlag, 2006).

3. Sessoli, R. Materials science: Magnetic molecules back in the race. *Nature* **548**, 400–401 (2017).

4. Liu, J.-L., Chen, Y.-C., Guo, F.-S. & Tong, M.-L. Recent advances in the design of magnetic molecules for use as cryogenic magnetic coolants. *Coord. Chem. Rev.* **281**, 26–49 (2014).

5. Jia, N., Banchi, L., Bayat, A., Dong, G. & Bose, S. Integrated information storage and transfer with a coherent magnetic device. *Sci. Rep.* **5**, 13665 (2015).

6. Mannini, M. *et al.* Magnetic memory of a single-molecule quantum magnet wired to a gold surface. *Nat. Mater.* **8**, 194–197 (2009).

7. Troiani, F., Carretta, S. & Santini, P. Detection of entanglement between collective spins. *Phys. Rev. B - Condens. Matter Mater. Phys.* **88**, 195421 (2013).

8. Aromí, G., Aguilà, D., Gamez, P., Luis, F. & Roubeau, O. Design of magnetic coordination complexes for quantum computing. *Chemical Society Reviews* **41**, 537–546 (2012).

9. Shiddiq, M. *et al.* Enhancing coherence in molecular spin qubits via atomic clock transitions. *Nature* **531**, 348–351 (2016).

10. Soncini, A. & Chibotaru, L. F. Molecular spintronics using noncollinear magnetic molecules. *Phys. Rev. B - Condens. Matter Mater. Phys.* **81**, 132403 (2010).

11. Bogani, L. & Wernsdorfer, W. Molecular spintronics using single-molecule magnets. *Nat. Mater.* **7**, 179–186 (2008).

12. Urdampilleta, M., Klyatskaya, S., Cleuziou, J.-P., Ruben, M. & Wernsdorfer, W. Supramolecular spin valves. *Nat. Mater.* **10**, 502–6 (2011).

13. Neese, F. Zero-Field Splitting. in *Calculation of NMR and EPR Parameters* 541–564 (Wiley-VCH Verlag GmbH & Co. KGaA, 2004). doi:10.1002/3527601678.ch34

14. Milios, C. J. *et al.* Toward a magnetostructural correlation for a family of Mn6 SMMs.

J. Am. Chem. Soc. **129**, 12505–12511 (2007).

15. Kostakis, G. E., Ako, A. M. & Powell, A. K. Structural motifs and topological representation of Mn coordination clusters. *Chem. Soc. Rev.* **39**, 2238–2271 (2010).

16. Zhang, P., Guo, Y. N. & Tang, J. Recent advances in dysprosium-based single molecule magnets: Structural overview and synthetic strategies. *Coordination Chemistry Reviews* **257**, 1728–1763 (2013).

17. Aromí, G. *et al.* Manganese carboxylate clusters: from structuralaesthetics to single-molecule magnets. *Polyhedron* **17**, 3005–3020 (1998).

18. Winpenny, R. E. P. High-nuclearity paramagnetic 3d-metal complexes with oxygen- and nitrogen-donor ligands. *Adv. Inorg. Chem.* **52**, 1–11 (2001).

19. Ardavan, A. *et al.* Engineering coherent interactions in molecular nanomagnet dimers. *npj Quantum Inf.* **1**, 15012 (2015).

20. Pugh, T. *et al.* Influencing the properties of dysprosium single-molecule magnets with phosphorus donor ligands. *Nat. Commun.* **6**, 7492 (2015).

21. Timco, G. A. *et al.* Engineering the coupling between molecular spin qubits by coordination chemistry. *Nat. Nanotechnol.* **4**, 173–178 (2009).

22. Gomez-Coca, S., Aravena, D., Morales, R. & Ruiz, E. Large magnetic anisotropy in mononuclear metal complexes. *Coord. Chem. Rev.* **289**, 379–392 (2015).

23. Bunting, P. C. *et al.* A linear cobalt(II) complex with maximal orbital angular momentum from a non-Aufbau ground state. *Science (80-.).* **362**, eaat7319 (2018).

24. Suturina, E. A., Maganas, D., Bill, E., Atanasov, M. & Neese, F. Magneto-Structural Correlations in a Series of Pseudotetrahedral [Co-II(XR)(4)](2-) Single Molecule Magnets: An ab Initio Ligand Field Study. *Inorg. Chem.* **54**, 9948–9961 (2015).

25. Rechkemmer, Y. *et al.* A four-coordinate cobalt(II) single-ion magnet with coercivity and a very high energy barrier. *Nat. Commun.* **7**, 10467 (2016).

26. Ziegenbalg, S., Hornig, D., Görls, H. & Plass, W. Cobalt(II)-Based Single-Ion Magnets with Distorted Pseudotetrahedral [N2O2] Coordination: Experimental and Theoretical Investigations. *Inorg. Chem.* **55**, 4047–4058 (2016).

27. Ferentinos, E. *et al.* Field-induced slow relaxation of magnetization in the S = 3/2 octahedral complexes trans -[Co{(OPPh 2)(EPPh 2)N} 2 (dmf) 2], E = S, Se: effects of Co–Se vs. Co–S coordination. *Inorg. Chem. Front.* (2019). doi:10.1039/c9qi00135b

28. Alvarez, S., Avnir, D., Llunell, M. & Pinsky, M. Continuous symmetry maps and shape classification. The case of six-coordinated metal compounds. *New J. Chem.* **26**, 996–1009 (2002).

29. Gatteschi, D., Sessoli, R. & Villain, J. *Molecular Nanomagnets*. *Molecular Nanomagnets* **9780198567**, (OUP Oxford, 2007).

30. Gómez-Coca, S. *et al.* Origin of slow magnetic relaxation in Kramers ions with non-uniaxial anisotropy. *Nat. Commun.* **5**, (2014).

31. Abragam, A. & Bleaney, B. (Brebis). *Electron paramagnetic resonance of transition ions*. (Oxford University Press, 1970).

32. Nehrkorn, J., Holldack, K., Bittl, R. & Schnegg, A. Recent progress in synchrotron-based frequency-domain Fourier-transform THz-EPR. *J. Magn. Reson.* **280**, 10–19 (2017).

33. Palacios, M. A. *et al.* Analysis of Magnetic Anisotropy and the Role of Magnetic Dilution in Triggering Single-Molecule Magnet (SMM) Behavior in a Family of CoIIYIII Dinuclear Complexes with Easy-Plane Anisotropy. *Chem. – A Eur. J.* **23**, 11649–11661 (2017).

34. Suturina, E. A. *et al.* Magneto-Structural Correlations in Pseudotetrahedral Forms of the [Co(SPh)4]2– Complex Probed by Magnetometry, MCD Spectroscopy, Advanced EPR Techniques, and ab Initio Electronic Structure Calculations. *Inorg. Chem.* **56**, 3102–3118 (2017).

35. Pilbrow, J. R. *Transition Ion Electron Paramagnetic Resonance*. (Clarendon Press, 1990).

36. Atanasov, M. *et al.* First principles approach to the electronic structure, magnetic anisotropy and spin relaxation in mononuclear 3d-transition metal single molecule magnets. *Coord. Chem. Rev.* **289**, 177–214 (2015).

37. Lunghi, A. & Sanvito, S. Surfing Multiple Conformation-Property Landscapes via Machine Learning: Designing Single-Ion Magnetic Anisotropy. *J. Phys. Chem. C* **0**, (2020).

38. Urtizberea, A. & Roubeau, O. Switchable slow relaxation of magnetization in the native low temperature phase of a cooperative spin-crossover compound. *Chem. Sci.* **8**, 2290–2295 (2017).

39. Craig, G. A. *et al.* Probing the origin of the giant magnetic anisotropy in trigonal bipyramidal Ni(ii) under high pressure. *Chem. Sci.* **9**, 1551–1559 (2018).

40. Fittipaldi, M. *et al.* Electric field modulation of magnetic exchange in molecular helices. *Nat. Mater.* **18**, 329–334 (2019).

41. Thiel, A. M., Damgaard-Møller, E. & Overgaard, J. High-Pressure Crystallography as a Guide in the Design of Single-Molecule Magnets. *Inorg. Chem.* **59**, 1682–1691 (2020).

42. Prescimone, A. *et al.* [Mn6] under pressure: A combined crystallographic and magnetic study. *Angew. Chemie - Int. Ed.* **47**, 2828–2831 (2008).

43. Sieber, A. *et al.* Effect of pressure on the magnetic anisotropy in the single-molecule magnet Mn12-acetate: An inelastic neutron scattering study. *Angew. Chemie - Int. Ed.* **44**, 4239–4242 (2005).

44. Bokach, N. A. *et al.* Co(II)-mediated and microwave assisted coupling between 2,6-diaminopyridine and nitriles. A new synthetic route to N-(6-aminopyridin-2-yl)carboximidamides. *Russ. Chem. Bull. (Translation Izv. Akad. Nauk. Seriya Khimicheskaya)* **55**, 36–43 (2006).

45. SMART (Control) and SAINT (Integration). (1997).

46. Sheldrick, G. M. SADABS, Program for Scaling and Correction of Area Detector Data. (1997).

47. Nehrkorn, J. *et al.* Zero-field splittings in metHb and metMb with aquo and fluoro ligands: a FD-FT THz-EPR study. *Mol. Phys.* **111**, 2696–2707 (2013).

48. Schnegg, A., Behrends, J., Lips, K., Bittl, R. & Holldack, K. Frequency domain Fourier transform THz-EPR on single molecule magnets using coherent synchrotron radiation. *Phys. Chem. Chem. Phys.* **11**, 6820 (2009).

49. Ivanov, M. Y. *et al.* Bismuth germanate as a perspective material for dielectric resonators in EPR spectroscopy. *J. Magn. Reson.* **271**, 83–89 (2016).

50. Nehrkorn, J., Telser, J., Holldack, K., Stoll, S. & Schnegg, A. Simulating Frequency-Domain Electron Paramagnetic Resonance: Bridging the Gap between Experiment and Magnetic Parameters for High-Spin Transition-Metal Ion Complexes. *J. Phys. Chem. B* **119**, 13816–13824 (2015).

51. Nehrkorn, J., Schnegg, A., Holldack, K. & Stoll, S. General magnetic transition dipole moments for electron paramagnetic resonance. *Phys. Rev. Lett.* **114**, 010801 (2015).

52. Stoll, S. & Schweiger, A. EasySpin, a comprehensive software package for spectral simulation and analysis in EPR. *J. Magn. Reson.* **178**, 42–55 (2006).

53. Roos, B. O., Taylor, P. R. & Siegbahn, P. E. M. A Complete Active Space Scf Method (Casscf) Using a Density-Matrix Formulated Super-Ci Approach. *Chem. Phys.* **48**, 157–173 (1980).

54. Siegbahn, P., Heiberg, A., Roos, B. & Levy, B. A Comparison of the Super-CI and the Newton-Raphson Scheme in the Complete Active Space SCF Method. *Phys. Scr.* **21**, 323–327 (1980).

55. Siegbahn, P. E. M., Almlof, J., Heiberg, A. & Roos, B. O. The Complete Active Space Scf (Casscf) Method in a Newton-Raphson Formulation with Application to the Hno Molecule. *J. Chem. Phys.* **74**, 2384–2396 (1981).

56. Pantazis, D. A., Chen, X. Y., Landis, C. R. & Neese, F. All-electron scalar relativistic basis sets for third-row transition metal atoms. *J. Chem. Theory Comput.* **4**, 908–919 (2008).

57. Schäfer, A., Horn, H. & Ahlrichs, R. Fully optimized contracted Gaussian basis sets for atoms Li to Kr. *J. Chem. Phys.* **97**, 2571–2577 (1992).

58. Weigend, F. & Ahlrichs, R. Balanced basis sets of split valence, triple zeta valence and quadruple zeta valence quality for H to Rn: Design and assessment of accuracy. *Phys. Chem. Chem. Phys.* **7**, 3297–3305 (2005).

59. Schäfer, A., Huber, C. & Ahlrichs, R. Fully Optimized Contracted Gaussian-Basis Sets of Triple Zeta Valence Quality for Atoms Li to Kr. *J. Chem. Phys.* **100**, 5829–5835 (1994).

60. Neese, F. An improvement of the resolution of the identity approximation for the formation of the Coulomb matrix. *J. Comput. Chem.* **24**, 1740–1747 (2003).

61. Angeli, C., Cimiraglia, R. & Malrieu, J. P. n-electron valence state perturbation theory: A spinless formulation and an efficient implementation of the strongly contracted and of the partially contracted variants. *J. Chem. Phys.* **117**, 9138–9153 (2002).

62. Angeli, C., Cimiraglia, R. & Malrieu, J. P. N-electron valence state perturbation theory: a fast implementation of the strongly contracted variant. *Chem. Phys. Lett.* **350**, 297–305 (2001).

63. Hess, B. A. Relativistic Electronic-Structure Calculations Employing a 2-Component No-Pair Formalism with External-Field Projection Operators. *Phys. Rev. A* **33**, 3742–3748 (1986).

64. Douglas, M. & Kroll, N. M. Quantum Electrodynamical Corrections to Fine-Structure of Helium. *Ann. Phys. (N. Y).* **82**, 89–155 (1974).

65. Ganyushin, D. & Neese, F. A fully variational spin-orbit coupled complete active space self-consistent field approach: Application to electron paramagnetic resonance g-tensors. *J. Chem. Phys.* **138**, 104113 (2013).

66. Neese, F. & Solomon, E. I. Calculation of zero-field splittings, g-values, and the relativistic nephelauxetic effect in transition metal complexes. Application to high-spin ferric complexes. *Inorg. Chem.* **37**, 6568–6582 (1998).

67. Maurice, R. *et al.* Universal theoretical approach to extract anisotropic spin hamiltonians. *J. Chem. Theory Comput.* **5**, 2977–2984 (2009).

68. Neese, F. The ORCA program system. *Wiley Interdiscip. Rev. Comput. Mol. Sci.* **2**, 73–78 (2012).

Figures

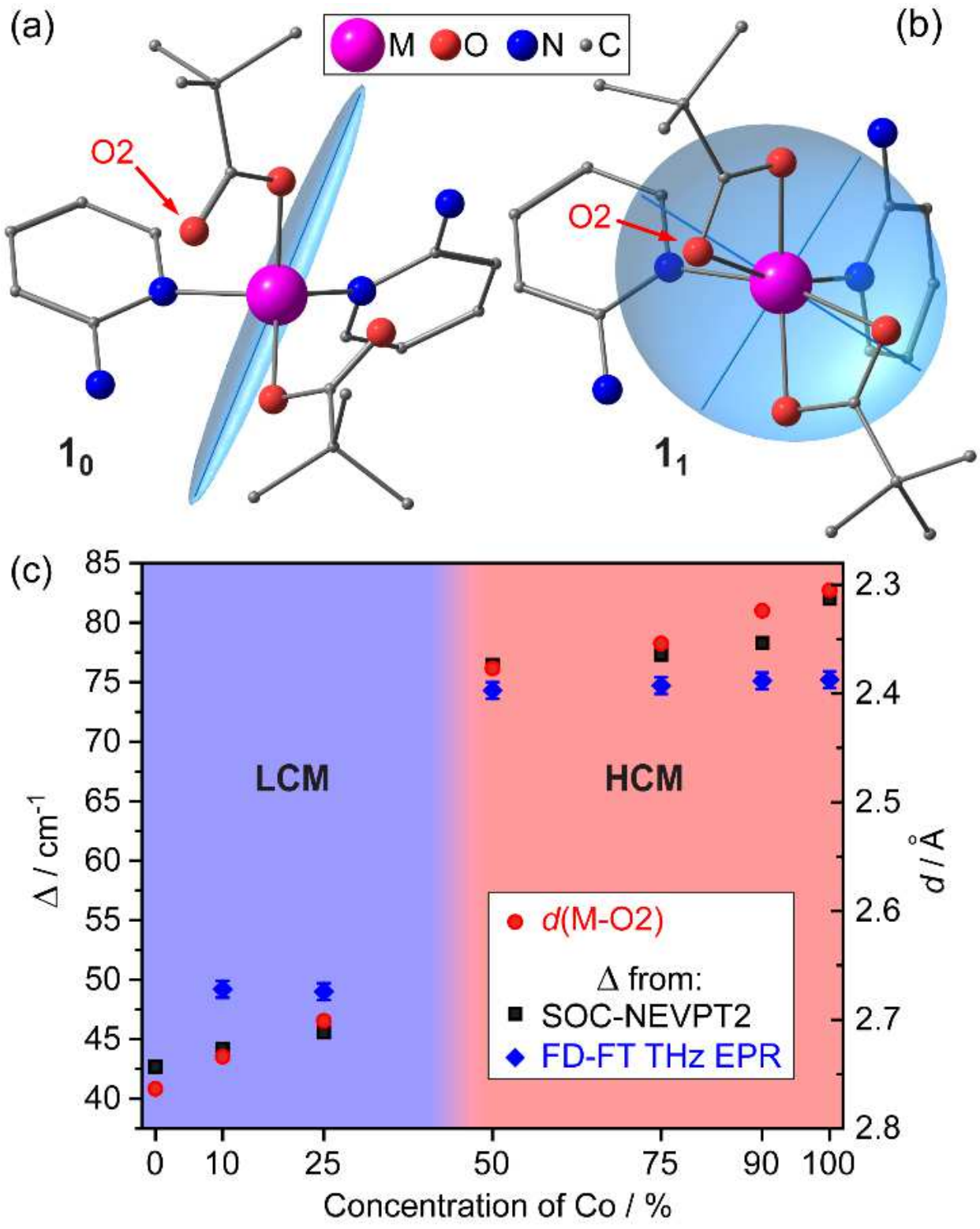

Figure 1

Host matrix induced changes of the ligand structure affect Co(II) magnetic anisotropy in Co depleted (LCM) and Co rich (HCM) materials. Molecular structures of 10 (a) and 11 (b), where M refers to the metal (either Co or Zn). Tensors representing the anisotropic response of the ground state Kramers doublet to a

magnetic field as calculated by SOC-NEVPT2 are shown in light blue. In 11 the metal ion has a distorted octahedral coordination environment and easy-plane anisotropy (i.e. an oblate tensor). 1o features a tetrahedral coordination environment and easy-axis anisotropy (prolate tensor). (c) Zero-field splitting Δ extracted from FD-FT THz-EPR experiments and calculated by SOC-NEVPT2. A steep increase of Δ with increasing Co(II) concentration can be observed around 50 % concentration. This anisotropy change correlates with bond lengths between the metal ion and the atoms in the first ligation shell. The bond length between metal and oxygen atom O2 is shown (red circles and y-scale on the right). Related plots for the remaining atoms in the first coordination shell are shown in the SI (see Table S3 and Figures S1 & S33).

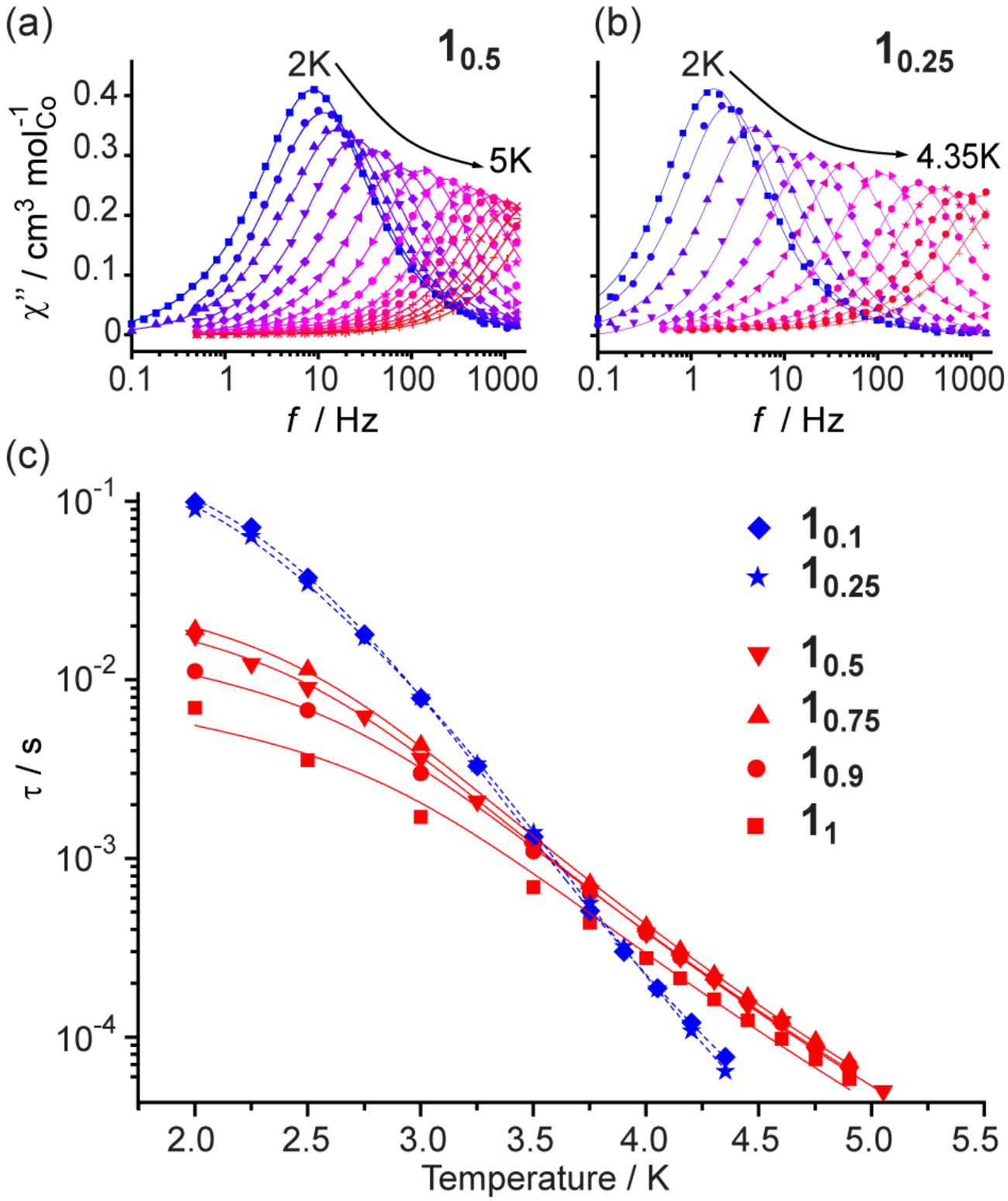

Figure 2

AC susceptibility data reveal a clear correlation between magnetic relaxation properties and magnetic anisotropies in HCM and LCM. (a) and (b) depict out-of-phase AC susceptibility traces, χ", vs. frequency, f, for 10.5 and 10.25. (c) Extracted relaxation times τ show different temperature dependencies for LCM (blue symbols) and HCM (red symbols).

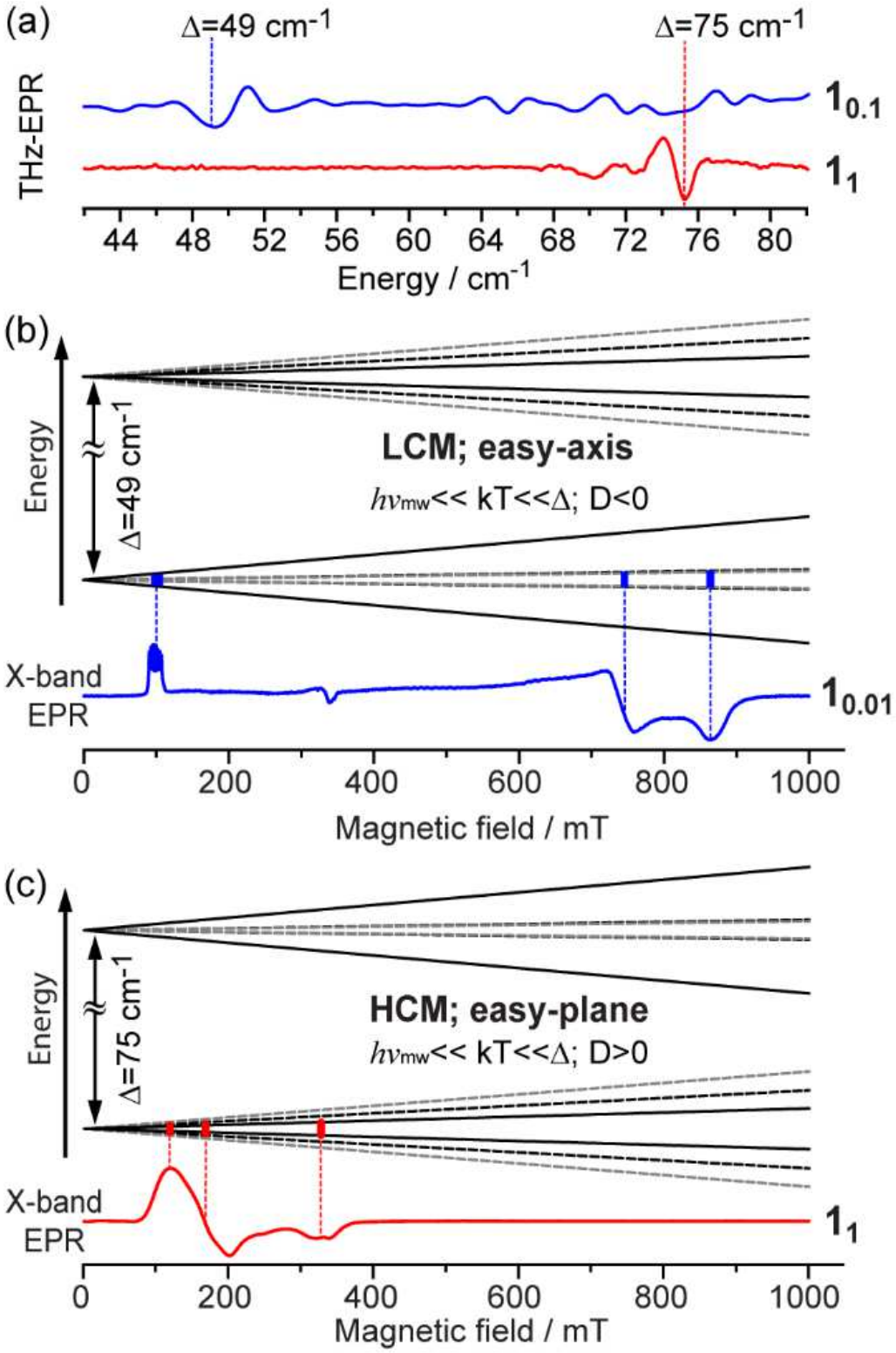

Figure 3

EPR allows for assigning magnitude and sign of the magnetic anisotropy of LCM and HCM. (a) THz-EPR quantifies = 75 cm-1 and Δ = 49 cm-1 for HCM (red) and LCM (blue), respectively. Δ is the energy gap between ground-state and excited-state doublets without external magnetic field, see (b) and (c). (b) Depicts magnetic field dependent S = 3/2 energy levels for easy-axis (D < 0) anisotropy alongside LCM X-band EPR spectra (blue trace). Ground-state and excited-state doublets are plotted for magnetic fields

parallel to the main anisotropy axis (solid black lines) and perpendicular to it (black and gray dashed lines). Resonance magnetic fields are assigned to the corresponding EPR transitions by blue dashed lines. (c) Orientation dependent spin energy levels and HCM X-band EPR spectrum (red trace) for easy-plane (D > 0). Resonance fields are assigned to EPR transitions by red dashed lines.

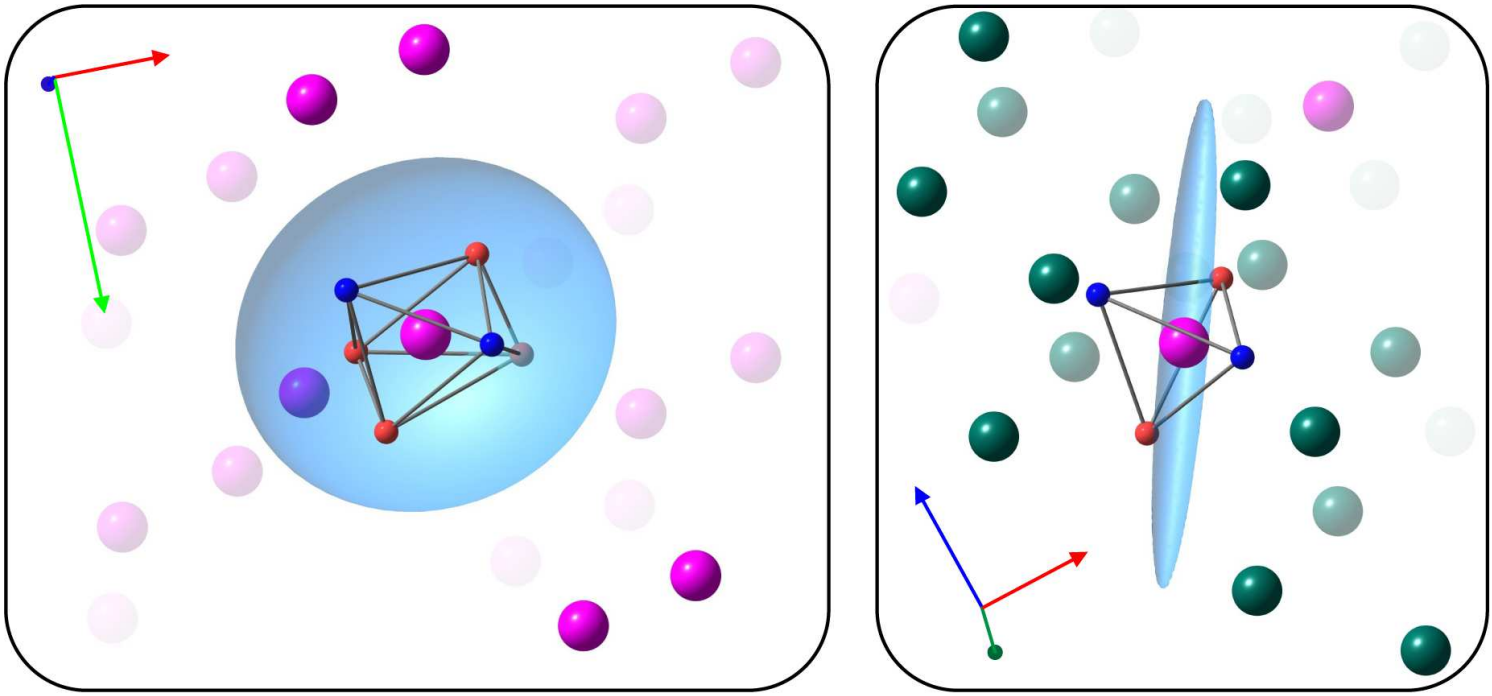

Figure 4

Schematic view of Co(II) (blue spheres) surrounded by other Co(II) (left, HCM) and Zn(II) (black spheres, right, LCM). In HCM, all or the majority of complexes contain Co(II), with distorted octahedral ligand environment and easy-plane type of anisotropy, depicted by an oblate tensor. In the LCM counterparts complexes molecules containing Co(II) are a minority. The remaining Co(II) are in a distorted tetrahedral ligand environment, resulting in easy-axis magnetic anisotropy (prolate tensor). Differences in the crystal packing and the size of the unit cell are indicated by different box sizes.

Supplementary Files

This is a list of supplementary files associated with this preprint. Click to download.

- nehrkornetal2020SI.pdf